28^{th} Symposium on Naval Hydrodynamics
Pasadena, California, 12-17 September 2010

Euler-Lagrangian Simulation of Bubble Migration in a Turbulent Boundary Layer

M. Mattson and K. Mahesh
(Aerospace Engineering and Mechanics, University of Minnesota)

ABSTRACT

One-way coupled Euler-Lagrangian simulations of bubbles in a spatially evolving turbulent boundary layer were performed. The simulation parameters were chosen to match an experiment by Sanders *et al.* (2006), though the Reynolds number of the boundary layer was lower than experiment. The bubbles were observed to migrate away from the wall, as observed in experiment. Budgets of the forces on the bubbles, along with PDFs of these forces, were computed. A simulation of bubbles in a spatially evolving laminar boundary layer was also performed. The role of turbulence in bubble migration away from the wall is demonstrated by the force budgets in turbulent flow and results from the laminar simulation.

INTRODUCTION

The presence of microbubbles in a turbulent flow has been shown to reduce skin-friction drag (McCormick & Bhattacharya, 1973). However, at large distances downstream from injection, the bubbles migrate away from the wall and drag reduction is lost (Sanders *et al.*, 2006), making microbubble induced drag reduction inefficient for large-scale vessels. Much of the work using DNS to simulate this flow has focused on the mechanisms of microbubble drag reduction (Xu *et al.*, 2002; Ferrante & Elghobashi, 2004; Ferrante & Elghobashi, 2005; Lu *et al.*, 2005). This work, using a one-way coupled, Euler-Lagrangian DNS approach, focuses on the mechanisms of microbubble dispersion away from the wall in a spatially evolving turbulent boundary layer. This paper is organized as follows. First, a description of the one-way coupled Euler-Lagrangian numerical approach is given. Also, the Sanders *et al*. (2006) experiment, along with our turbulent boundary layer simulation, is described. Results for bubble trajectories, forces on the bubbles and force budgets are then shown, followed by a discussion of the role of turbulence on bubble migration away from the wall.

DESCRIPTION OF PROBLEM

Sanders *et al.* (2006) performed experiments of microbubble skin-friction drag reduction in a high Reynolds number, spatially evolving turbulent boundary layer and found that microbubble skin-friction drag reduction, though effective near the bubble injection location, lost its effectiveness far downstream from injection. Skin-friction drag reduction is measured by the ratio of skin-friction (C_f) of the bubbly flow to the skin-friction without bubbles ($C_{f,0}$). In this experiment, air was injected at various rates through porous plates into the fully developed boundary layer at a streamwise distance of $x = X_{\text{inj}}$ and measurements of skin friction and bubble locations were made at various downstream locations ($x = X_1, X_2,$ etc.). Figure 1 shows the typical bubble behavior in this experiment, with the boundary layer on the underside of the plate.

In general, increasing the air flow-rate of injection, Q_a, and/or reducing free-stream velocity, U_e, increased microbubble drag reduction. For cases with the lowest free-stream velocity, the bubbles coalesced into a continuous layer of gas and drag reduction was maintained far downstream. For all other free-stream speeds and air-injection rates, the skin-friction drag was reduced downstream ($C_f/C_{f,0} < 1$) of the bubble injection location, but increased with downstream distance and approached single-phase levels ($C_f/C_{f,0} \rightarrow 1$). In these experiments, the near-wall bubble concentration became more dilute with downstream distance and eventually a bubble-free liquid layer formed near the wall. Using the Euler-Lagrangian model, we performed simulations of bubbles injected into a spatially evolving turbulent boundary layer to describe the mechanisms behind bubble migration away from the wall.

For the low air-injection rate ($Q_{\text{a}} = 0.05$ m^{3}s^{-1}) and high flow speed ($U_e > 18$ ms^{-1}) in the Sanders *et al.* (2006) experiments, the skin-friction reduction as compared to the single-phase case was very small ($C_f/C_{f,0} > 0.95$) for small distances downstream ($x < 2$ m) and approached single-phase results further downstream. This experiment will now be defined as case S1.

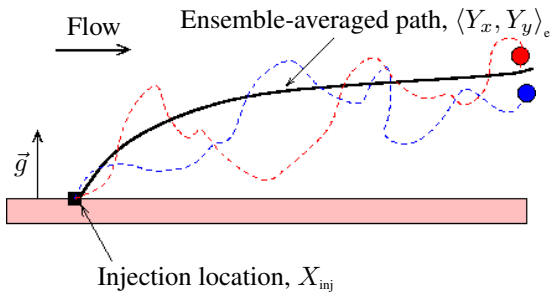

Figure 1: Schematic of boundary layer and bubble paths. Colored dashed lines denote the instantaneous path taken by a like-colored bubble and the black line represents the ensemble-averaged path of all bubbles.

Due to the large Reynolds numbers in this turbulent boundary layer ($Re_\theta > 15,000$), providing sufficient resolution of the turbulent flow with DNS is prohibitively expensive. The Reynolds number of the boundary layer is reduced ($420 < Re_\theta < 1500$) in these simulations while matching the ratio of mean bubble injection radius to boundary layer size at injection. For experiment S1, the mean bubble radius and boundary layer thickness were given at downstream station X_1. Assuming a constant bubble radius and using a power law to estimate boundary layer thickness, the ratio of bubble size to boundary layer thickness at injection is obtained ($R_{\text{inj}}/\delta_{99,\text{inj}} \approx 0.0064$) and matched in the simulation. The distance between X_1 and X_{inj}, non-dimensionalized by the boundary layer thickness (δ_{99}) at injection, is 35.6 for experiment and simulation. The bubble injection velocity is zero in the streamwise and spanwise directions and the wall normal injection velocity, v_y/U_e, is 0.55, as given in the Sanders (2004) model of microbubble injection in a turbulent boundary layer. The Froude number ($\text{Fr} = U_e/\sqrt{g_y \delta_{99,\text{inj}}}$) is 45.7, as in experiment.

NUMERICAL APPROACH

In the one-way coupled Euler-Lagrangian framework, the bubbles are modeled as a dispersed phase, with individual bubbles treated as point particles governed by an equation for bubble motion, combined with a continuous carrier phase described by DNS / LES Navier-Stokes equations. To solve the Navier-Stokes equations for the continuous phase, a finite-volume approach for unstructured grids (Mahesh *et al.*, 2004) is used. This algorithm assumes constant density of the carrier phase and solves the incompressible Navier-Stokes equations using a predictor-corrector approach. This algorithm is discretely energy conserving to ensure robustness at high Reynolds numbers. This method is able to simulate large numbers of bubbles in complex flows. Each bubble is tracked individ-

Table 1: Simulation Domains

Case	$L_x \times L_y \times L_z$	$N_x \times N_y \times N_z$
bubbly flow	$40 \times 3.12 \times 1.57$	$1600 \times 132 \times 256$
inflow gen.	$10 \times 3.12 \times 1.57$	$100 \times 45 \times 64$

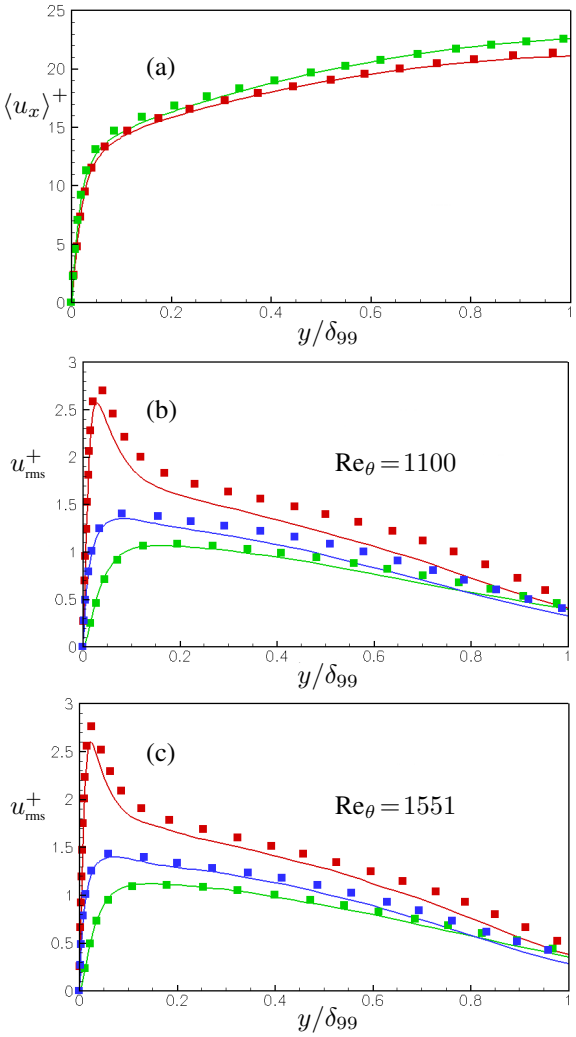

Figure 2: Comparison of mean streamwise velocity and turbulence intensities to results from the Simens *et al.* (2009) simulation. —, DNS; ■, Simens *et al.* (a) Mean streamwise velocity versus wall-normal distance. —, $\text{Re}_\theta = 1100$; —, $\text{Re}_\theta = 1551$. (b), (c) RMS of the turbulence intensities versus wall-normal distance. —, $u^+_{x,\text{rms}}$; —, $u^+_{y,\text{rms}}$; —, $u^+_{z,\text{rms}}$.

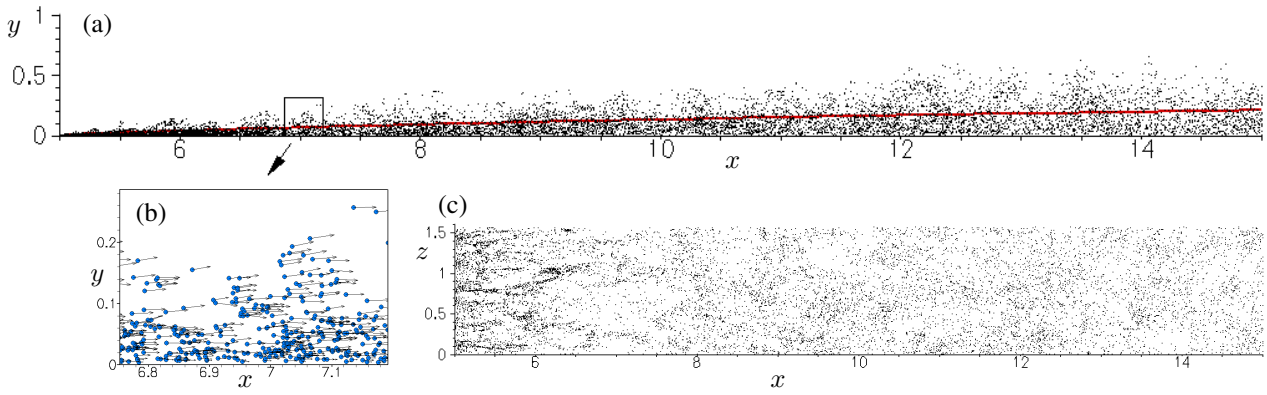

Figure 3: Instantaneous bubble position with only the first half shown $(0 < x < 15)$. (a) Position in streamwise and wall-normal coordinates with ensemble-averaged position $\langle Y_y \rangle_e$ vs. $\langle Y_x \rangle_e$ shown by the red line. (b) Close-up view of (a) along with bubble velocity vectors (v_x, v_y). (c) Position in streamwise and spanwise coordinates.

ually and is characterized by its instantaneous position, velocity and size.

Various forces from the carrier fluid act upon the bubble and are applied to the bubble's center of mass. The bubble is assumed to be much smaller than the length scales of motion in the carrier phase and the bubbles are modeled as spherical nuclei. Due to a bubble's small size and assuming a dilute concentration of bubbles, the bubbles exert a negligible force on the carrier fluid and other bubbles. This is the one-way coupling regime. The bubble acceleration is equal to sum of the forces on the bubble. These forces are the drag, lift, fluid acceleration, buoyancy and added-mass forces (Johnson & Hsieh, 1966; Thomas *et al.*, 1984; Auton *et al.*, 1988), yielding

$$m_{\mathrm{b}} \frac{d\vec{v}}{dt} = \sum \vec{F} = \vec{F}_{\mathrm{D}} + \vec{F}_{\mathrm{L}} + \vec{F}_{\mathrm{F}} + \vec{F}_{\mathrm{B}} + \vec{F}_{\mathrm{AM}},$$

with m_{b} defined as the mass of the bubble and $\vec{v}$ as the bubble velocity. The forces on the bubble are described by the following equations:

$$\begin{aligned}
\vec{F}_{\mathrm{D}} &= \frac{1}{2}\rho_{\mathrm{f}} A_{\mathrm{b}} C_{\mathrm{D}} \left|\vec{u} - \vec{v}\right| (\vec{u} - \vec{v}) \\
\vec{F}_{\mathrm{L}} &= m_{\mathrm{f}} C_{\mathrm{L}} (\vec{u} - \vec{v}) \times \vec{\omega} \\
\vec{F}_{\mathrm{F}} &= m_{\mathrm{f}} \frac{D\vec{u}}{Dt} \\
\vec{F}_{\mathrm{B}} &= (m_{\mathrm{b}} - m_{\mathrm{f}})\, \vec{g} \\
\vec{F}_{\mathrm{AM}} &= m_{\mathrm{f}} C_{\mathrm{M}} \left(\frac{D\vec{u}}{Dt} - \frac{d\vec{v}}{dt} \right) + 4\pi R^2 \rho_{\mathrm{f}} C_{\mathrm{M}} (\vec{u} - \vec{v}) \frac{dR}{dt},
\end{aligned}$$

where the carrier-phase velocity, $\vec{u}$, is interpolated to the bubble's instantaneous position and A_{b} is the area of a circle with radius R, the bubble radius. The carrier-phase density is defined as ρ_{f} and the equivalent mass of a sphere with radius R and the density of the carrier-phase is m_{f}. A constant lift coefficient, C_{L}, of 0.5 (Auton, 1987) and a constant added-mass coefficient, C_{M}, of 0.5 (Batchelor, 1967) are used.

Contributions to the added-mass force due to changes in relative velocity (Batchelor, 1967) and changes in bubble volume (Lhuillier, 1982) are important in bubbly flows because the mass of the bubble is very small compared to the carrier fluid. The material derivative of the fluid velocity is obtained at the bubble center using a tri-linear interpolation in space and linear interpolation in time by

$$\left.\frac{Du_i}{Dt}\right|_{\vec{Y}(t)} = \left.\left(\frac{\partial u_i}{\partial t} + u_j \frac{\partial u_i}{\partial x_j}\right)\right|_{\vec{x}=\vec{Y}(t)}, \qquad (1)$$

and the fluid velocity, pressure and vorticity are also interpolated to the instantaneous bubble location using a trilinear method. The following expression for bubble drag, a function of bubble Reynolds number and determined experimentally by Haberman & Morton (1953), is used:

$$C_{\mathrm{D}} = \frac{24}{\mathrm{Re}_{\mathrm{b}}} \left(1.0 + 0.197\mathrm{Re}_{\mathrm{b}}^{0.63} + 2.6\times10^{-4}\mathrm{Re}_{\mathrm{b}}^{1.38}\right), \quad (2)$$

where the bubble Reynolds number (Re_{b}) is defined as $2R\left|\vec{u} - \vec{v}\right|/\nu$. For small bubbles in water, the drag profile is similar to that of solid spheres ($C_{\mathrm{D}} \sim 24/\mathrm{Re}_{\mathrm{b}}$), due to the contamination by surfactants of the bubble surface.

Assuming that the density of gas inside a bubble is much less than that of water, the bubble mass m_{b} is much less than m_{f} and the sum of forces on a bubble is zero. After substituting the above expressions for bubble forces into Eqn. 1, the following expression is obtained

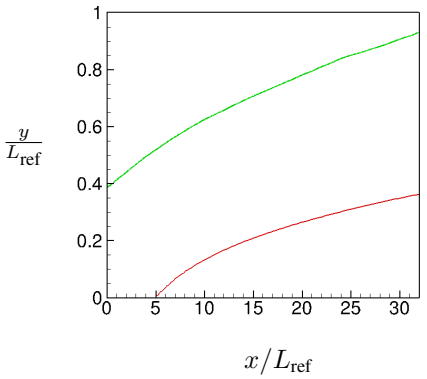

Figure 4: Ensemble-averaged bubble trajectory as compared to boundary-layer thickness. —, δ_{99} vs. x; —, $\langle Y_y \rangle_{\text{e}}$ vs. $\langle Y_x \rangle_{\text{e}}$

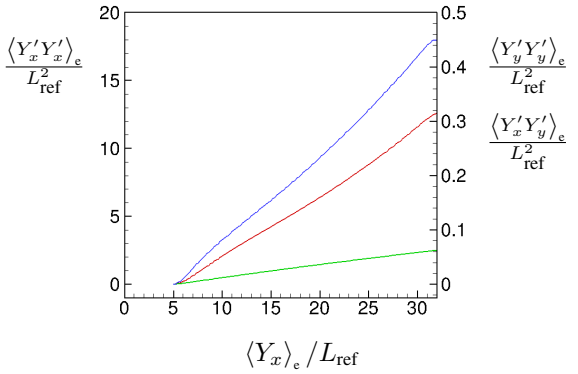

Figure 6: Ensemble-averaged position fluctuations. —, $\langle Y'_x Y'_x \rangle_{\text{e}}$; —, $\langle Y'_y Y'_y \rangle_{\text{e}}$; —, $\langle Y'_x Y'_y \rangle_{\text{e}}$.

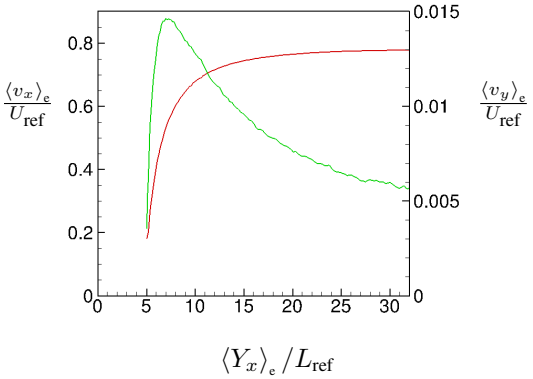

Figure 5: Ensemble-averaged bubble velocities. —, $\langle v_x \rangle_{\text{e}}$; —, $\langle v_y \rangle_{\text{e}}$.

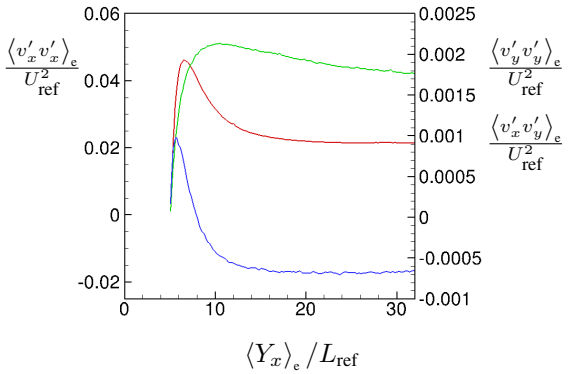

Figure 7: Ensemble-averaged velocity fluctuations. —, $\langle v'_x v'_x \rangle_{\text{e}}$; —, $\langle v'_y v'_y \rangle_{\text{e}}$; —, $\langle v'_x v'_y \rangle_{\text{e}}$.

for the time derivative of the bubble velocity:

$$\frac{d\vec{v}}{dt} = \underbrace{-2\vec{g}}_{\text{Buoyancy}} + \underbrace{3\frac{D\vec{u}}{Dt}\Big|_{\vec{Y}(t)}}_{\text{Fluid material derivative}} + \underbrace{\frac{3}{4}\frac{C_{\text{D}}}{R}|\vec{u}-\vec{v}|(\vec{u}-\vec{v})}_{\text{Drag}} + \underbrace{2C_{\text{L}}[(\vec{u}-\vec{v})\times\vec{\omega}]}_{\text{Lift}} + \underbrace{\frac{3}{R}(\vec{u}-\vec{v})\frac{dR}{dt}}_{\text{Volumetric}}. \quad (3)$$

The Rayleigh-Plesset equation is used to determine the instantaneous bubble radius as a function of pressure in the carrier fluid. A fourth-order Runge-Kutta solver with adaptive time-stepping is used to ensure accurate and efficient integration of the Rayleigh-Plesset equation. A 2nd-order Adams-Bashforth time integrator is used to advance the bubble position in time.

This approach can simulate flows with large numbers of bubbles in complex geometries over a wide range of Reynolds numbers. By using the Rayleigh-Plesset (RP) equation to determine the radial response of the bubble, this model can be extended to flows with large pressure fluctuations (such as cavitating flows). Including the RP ordinary differential equation provides some numerical challenges when solving systems with large numbers of bubbles, since it must be solved for each individual bubble. The bubble oscillation timescales can become much smaller than the timescales of the carrier fluid. To solve the RP equation, a variable-timestepping fourth-order accurate (in time) Runge-Kutta integration scheme is applied. This allows resolution of the small bubble timescales during rapid growth and collapse with small, accurate timesteps and also boosts efficiency by increasing the timestep when the bubble is near equilibrium (Babu, 2007). For these simulations, the bubble size variation is ignored and the bubble is assumed to be a solid, massless sphere. Bubble-wall interactions are treated as hard-sphere, inelastic collisions. For dilute bubbly flows, bubble-bubble interactions are negligible and ignored.

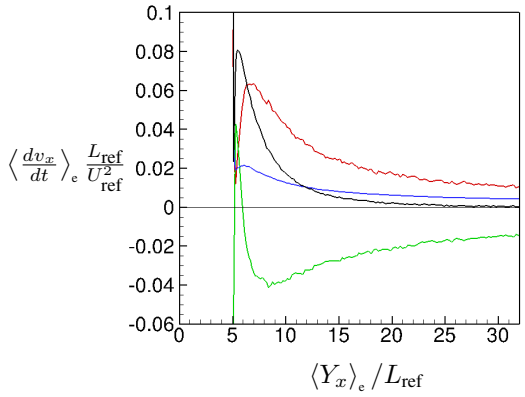

Figure 8: Ensemble-averaged bubble acceleration budget in the streamwise (x) direction. The thin black line denotes zero for the y-axis. —, Drag$_x$; —, $3\frac{Du_x}{Dt}$; —, Lift$_x$; —, Total$_x$.

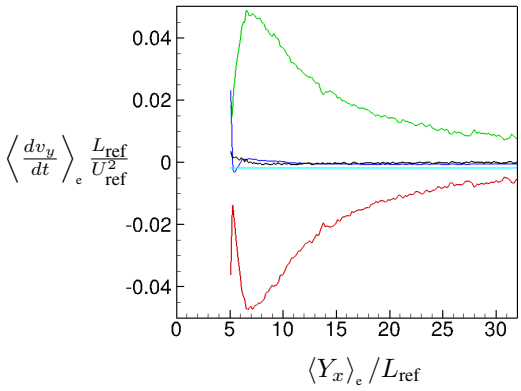

Figure 9: Ensemble-averaged bubble acceleration budget in the wall-normal (y) direction. —, Drag$_y$; —, $3\frac{Du_y}{Dt}$; —, Lift$_y$; —, $-2g$; —, Total$_y$.

TURBULENT BOUNDARY LAYER SIMULATION

A separate simulation is required to provide the necessary inflow turbulence for the spatially-evolving turbulent boundary layer simulation. The inflow generation simulation applies rescaling to the streamwise boundary conditions (Lund, 1998) to obtain turbulent boundary layer flow in a reasonably-sized domain. A velocity plane from the inflow simulation is then interpolated to the inflow plane of the bubbly-flow simulation. The domain lengths (L) and number of control volumes (N) in the x (streamwise), y (wall-normal) and z (spanwise) directions are given in Table 1. The bulk Reynolds number, $\mathrm{Re} = U_e L_{\mathrm{ref}}/\nu$ is equal to 14000, with $U_e = U_{\mathrm{ref}} = 1$ and $L_{\mathrm{ref}} = \delta_{99,\mathrm{inj}}/0.52$. At the inflow of the inflow generation simulation, the Reynolds number based on the momentum thickness (Re_θ) is 420. The grid spacing is uniform in the streamwise and spanwise directions and non-uniform in the wall-normal direction. For the bubbly-flow domain, $\Delta y_{\mathrm{min}} = 5.07 \times 10^{-4}$, with $\Delta y^+_{\mathrm{min}} = 0.31$ and 13 control volumes within $\Delta y^+ < 10$ at $(x - X_{\mathrm{inj}})/\delta_{99,\mathrm{inj}} = 45.4$. For the inflow generation domain, $\Delta y_{\mathrm{min}} = 1.96 \times 10^{-3}$, with $\Delta y^+_{\mathrm{min}} = 1.38$ and 6 control volumes within $\Delta y^+ < 10$ at $(x - X_{\mathrm{inj}})/\delta_{99,\mathrm{inj}} = -9.6$.

The inflow generation simulation was initialized from a previous boundary layer simulation and run for $t^* = tL_{\mathrm{ref}}/U_{\mathrm{ref}} = 422$ units of time to ensure removal of all transients, with a $\Delta t^* = 0.08$. Statistics were taken from $422 < t^* < 4398$, and the velocity inflow plane and additional statistics were sampled from $4398 < t^* < 8873$. The bubbly-flow simulation was initialized from zero velocity and run for 1370 units of time to remove all transients, with $\Delta t^* = 0.015$. One-hundred bubbles were then injected every 10 fluid timesteps at a random spanwise location near the wall ($y_{\mathrm{inj}}/\delta_{99,\mathrm{inj}} = 2 \times 10^{-6}$) and fluid statistics and bubble statistics were sampled from $1370 < t^* < 2135$ until convergence was achieved.

Results for the carrier-phase turbulent flow in the bubbly-flow simulation are given in Figure 2. The results shown are taken from two streamwise locations, one at $\mathrm{Re}_\theta = 1100$ and another at $\mathrm{Re}_\theta = 1551$. The wall-normal distance is non-dimensionalized by the boundary layer thickness, δ_{99}, at each streamwise location. The carrier flow shows reasonable agreement with the Simens *et al.* simulations for both the mean flow and turbulent intensities, though the downstream results ($\mathrm{Re}_\theta = 1551$) agree better than results for $\mathrm{Re}_\theta = 1100$.

RESULTS

BUBBLE TRAJECTORIES

Injected bubbles travel downstream and disperse due to the turbulent flow acting upon them through the lift, drag, fluid acceleration, buoyancy and added-mass forces. The bubbles tend to disperse and travel away from the wall, as shown in the instantaneous snapshots of bubble position in Figure 3. The bubbles concentrate into filament-like structures that break up with increasing downstream distance. The formation of these structures has been observed in previous simulations of bubbles in homogeneous, isotropic turbulence (Maxey *et al.*, 1996). The bubbles also tend to travel away from the wall as they move downstream, as observed in the Sanders *et al.* (2006) ex-

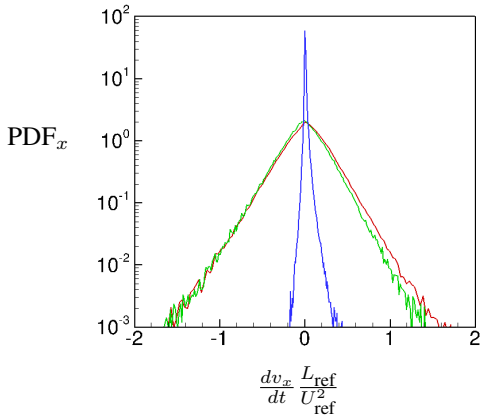

Figure 10: PDF of bubble acceleration terms in the streamwise (x) direction at $(t\,U_{\text{ref}})\,/L_{\text{ref}} = 30$. —, Drag$_x$; —, $3\frac{Du_x}{Dt}$; —, Lift$_x$.

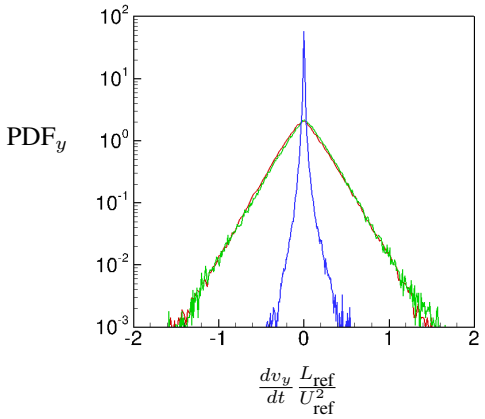

Figure 11: PDF of bubble acceleration terms in the wall-normal (y) direction at $(t\,U_{\text{ref}})\,/L_{\text{ref}} = 30$. —, Drag$_y$; —, $3\frac{Du_y}{Dt}$; —, Lift$_y$.

periment. Figure 4 shows the ensemble-averaged bubble trajectory, with the tendency of the bubbles to travel away from the wall clearly evident. Ensemble-averaging was performed by sampling bubble forces, positions, etc., at specific intervals in time and averaging the sampled quantity (for each time interval) over all bubbles. Ensemble-averaged quantities are denoted by brackets with the subscript 'e.'

Figure 5 plots the ensemble-averaged bubble velocities and time from injection as a function of ensemble-averaged streamwise position. In the mean, as the bubbles travel downstream, the streamwise velocity is increased, due to the bubbles accelerating along with the fluid as they enter the higher-momentum flow away from the wall. The wall-normal velocity is positive (away from the wall) and decreases as the bubbles travel downstream.

The ensemble-averaged fluctuations of bubble position and velocity are plotted in Figures 6 and 7. Streamwise fluctuations are large as compared to wall-normal position fluctuations, due to the large velocity fluctuations along the streamwise direction. The fluctuations in position increase with downstream distance due to dispersion. The bubble velocity fluctuations increase to a maximum value just downstream of injection then decrease and approach a constant value as the bubble travels downstream.

FORCES ON BUBBLES

Budgets of mean bubble acceleration as a function of time from injection for bubbles in the turbulent boundary layer are shown in Figures 8 and 9. The terms plotted are the ensemble-averaged contributions from drag, lift, fluid acceleration and gravity from Eqn. 3. For the streamwise accelerations, the drag and lift contributions accelerate the bubble in the positive downstream direction while the fluid acceleration tends to slow the bubbles, except for a short period after injection where the fluid acceleration is positive. The drag acceleration is positive, therefore the difference in velocity in the streamwise direction, $\langle u_x \rangle_e - \langle v_x \rangle_e$, is greater than zero. The streamwise ensemble-averaged bubble acceleration is always positive and approaches zero for large times after injection.

The wall-normal accelerations also include a gravitational term that acts to push the bubbles towards the wall, as in the experiment. However, this term is very small with respect to the other forces on the bubble. The drag and lift forces accelerate the bubble towards the wall, while the fluid acceleration pushes the bubble away from the wall. The lift acceleration is small compared to the fluid acceleration and drag. From the drag force, the difference in velocity in the wall-normal direction, $\langle u_y \rangle_e - \langle v_y \rangle_e$, is less than zero, so the bubble (in an ensemble-averaged sense) has a larger wall-normal velocity than the Eulerian fluid. The ensemble-averaged bubble acceleration in the wall-normal direction is negative (except very near injection) and approaches zero at large times from injection.

The forces acting on the bubbles in the turbulent boundary layer are very intermittent. Figures 10 and 11 plot the probability density function (pdf) of the acceleration terms from Eqn. 3. In both figures, the drag and fluid accelerations are the most intermittent and the lift acceleration is the least. For both the x and y directions, the pdfs of drag and fluid acceleration are symmetric about the mean, while the pdf of the lift force in x-direction is

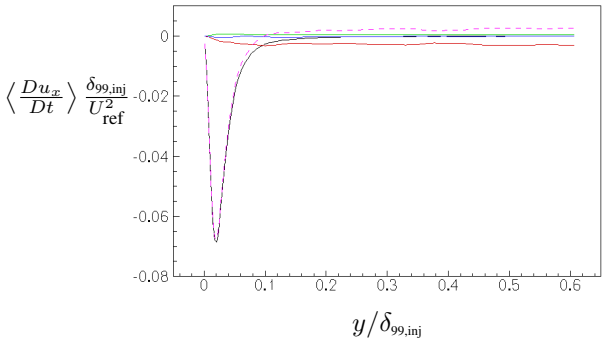

Figure 12: Time and spatially-averaged fluid material derivative budget in the streamwise (x) direction. Spatial averaging was performed in the z-direction. —, $\langle u_x \rangle \frac{\partial \langle u_x \rangle}{\partial x}$; —, $\langle u_y \rangle \frac{\partial \langle u_x \rangle}{\partial y}$; —, $\frac{\partial}{\partial x} \langle u_x' u_x' \rangle$; - -, $\frac{\partial}{\partial y} \langle u_x' u_y' \rangle$; —, $\left\langle \frac{du_x}{dt} \right\rangle$.

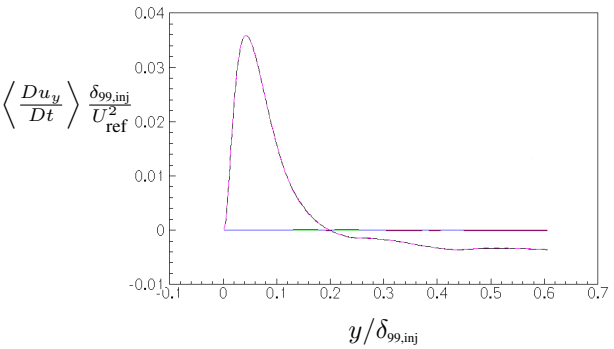

Figure 13: Time and spatially-averaged fluid material derivative budget in the wall-normal (y) direction. Spatial averaging was performed in the z-direction. —, $\langle u_x \rangle \frac{\partial \langle u_y \rangle}{\partial x}$; —, $\langle u_y \rangle \frac{\partial \langle u_y \rangle}{\partial y}$; —, $\frac{\partial}{\partial x} \langle u_x' u_y' \rangle$; - -, $\frac{\partial}{\partial y} \langle u_y' u_y' \rangle$; —, $\left\langle \frac{du_y}{dt} \right\rangle$.

skewed towards the positive direction, though the mean is negative. The standard deviation of the drag and fluid accelerations are an order of magnitude larger than the mean quantities of each acceleration contribution, while the standard deviation of the lift acceleration is the same order of magnitude as the mean. Having such large intermittency in the forces on the bubble produces large fluctuations of bubble velocity and results in the increase of bubble dispersion as the bubbles travel downstream with the flow.

BUDGET OF CARRIER-PHASE MATERIAL DERIVATIVE

The material derivative of the carrier fluid is a significant force on a bubble in a turbulent flow. It is especially large near the wall, a region with large turbulent fluctuations. The turbulence contributes significantly to the fluid acceleration. Taking a time average of the material derivative of the Eulerian velocity field, we obtain

$$\left\langle \frac{Du_i}{Dt} \right\rangle = \frac{\partial \langle u_i \rangle}{\partial t} + \langle u_j \rangle \frac{\partial \langle u_i \rangle}{\partial x_j} + \frac{\partial}{\partial x_j} \langle u_i' u_j' \rangle , \quad (4)$$

where the unsteady term is zero for statistically stationary flow. To highlight the importance of the turbulence, the time-averaged material derivative terms from Eqn. 4 were obtained at the injection location, X_{inj}, and plotted as a function of wall-normal distance in Figures 12 and 13. The velocity terms were sampled every five timesteps at each control volume during the simulation until statistical convergence was reached, then these statistics were averaged along the statistically homogeneous (spanwise) direction.

Near the wall ($y/\delta_{99,\text{inj}} < 0.1$) the wall-normal Reynolds stress term $\frac{\partial}{\partial y} \langle u_x' u_y' \rangle$ dominates the streamwise velocity material derivative and the total material derivative is negative. As y increases, this term becomes positive and is near the same order of magnitude (but opposite sign) as the $\langle u_x \rangle \frac{\partial \langle u_x \rangle}{\partial x}$ term, where $\langle u_x \rangle \frac{\partial \langle u_x \rangle}{\partial x}$ is negative due to boundary layer growth. For the wall-normal velocity material derivative, the $\frac{\partial}{\partial y} \langle u_y' u_y' \rangle$ term dominates throughout the boundary layer, with a positive value near the wall ($y/\delta_{99,\text{inj}} < 0.2$), then negative away from the wall. From these results it is clear that the contribution of turbulence to bubble acceleration is significant.

ROLE OF TURBULENCE

Turbulence significantly affects bubble dispersion in a turbulent boundary layer. Without these terms there is a lack of intermittency of the forces on the bubbles and no migration of bubbles away from the wall. To demonstrate this, we performed a simulation of bubbles injected into a laminar boundary layer. The outer scales were matched between the turbulent and laminar simulations at the injection location, with $\text{Re} = 14000$ and $R/\delta_{99,\text{inj}} = 0.0064$. The bubble radius was kept constant throughout the simulation. A simulation domain of $L_x = 40, L_y = 3.12$ and $L_z = 1.57$ was used, with $N_x = 400, N_y = 45$ and $N_z = 64$. The grid was uniform in the streamwise and spanwise directions, but non-uniform in the wall-normal direction with smaller spacing near the wall. The simulation was initialized with the Blasius solution (Schlichting, 1968) and then advanced until the velocity field was converged. Good agreement between velocity field and Blasius solution was obtained.

In this laminar flow, the forces on the bubble are greatly simplified as compared to turbulent flow, with no fluctuating terms in the accelerations equations. The bubble is injected with a positive wall-normal velocity, and travels slightly into the boundary layer (Figure 14). The bubble penetrates only a small distance into the boundary layer due to drag and then travels towards the wall, oppo-

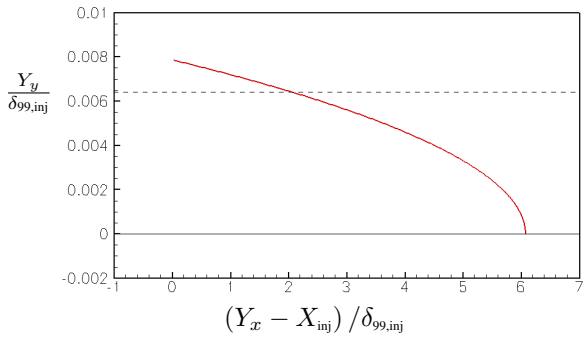

Figure 14: Bubble trajectories in the laminar boundary layer, non-dimensionalized by streamwise injection location (X_{inj}) and boundary layer thickness at injection ($\delta_{99,\text{inj}}$). Wall-normal distance equal to the size of the bubble radius is represented by the dashed line.

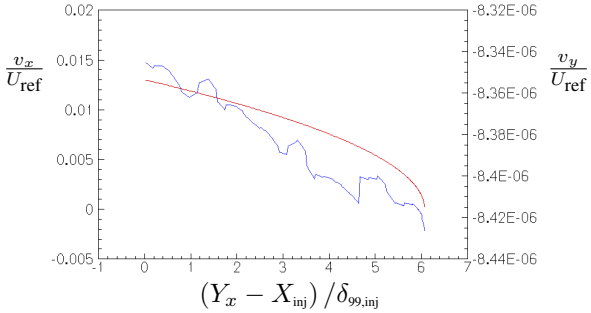

Figure 15: Bubble velocities in the laminar boundary layer. —, $\langle v_x \rangle_e / U_{\text{ref}}$; —, $\langle v_y \rangle_e / U_{\text{ref}}$.

site of what is seen in the turbulent case. Because the size of the bubble is on the same scale as the penetration distance, the distance from the wall equal to the bubble radius is plotted by the dashed line in Figure 14. The simulation was allowed to continue to run without any particle-wall boundary conditions (such as bubble-wall collisions) until the bubble center reached the wall itself. Bubble-wall interactions were ignored.

As seen in Figure 17, the forces on the bubble are constant throughout the bubble path, except very near injection where a large drag force quickly damps out the initial injection velocity of the bubble. This happens very quickly with respect to the other scales in the flow and is not shown in Figure 17 or the other figures of laminar flow. The lift force and fluid acceleration are both zero and the drag exactly counterbalances the buoyancy force. The bubble has reached its terminal velocity according to the equation

$$\frac{dv_y}{dt} = -2g + \frac{3}{4}\frac{C_{\text{D}}}{R}\left|\vec{u} - \vec{v}\right|\left(\vec{u} - \vec{v}\right)_y ,$$

and since the terms on the right-hand side balance each other at steady state and $C_{\text{D}} \sim 24/\text{Re}_{\text{b}}$,

$$2g = \frac{9\nu}{R^2}\left(u_y - v_y\right)$$

and the bubble has a constant velocity in the wall normal direction of $v_y/U_{\text{ref}} = 8.4 \times 10^{-5}$ since $u_y \approx 0$ near the wall, as seen in Figure 15. The streamwise velocity decreases as the bubble travels downstream. The carrier-phase streamwise velocity decreases and goes to zero as the wall is approached, as does the bubble streamwise velocity. The bubble acceleration in the streamwise direction is shown in Figure 16. The fluid acceleration and drag are near zero, but a lift force pushes the bubble towards the wall. This is described by the equation

$$\begin{aligned} \frac{dv_x}{dt} &= 2C_{\text{L}}\left[\left(\vec{u} - \vec{v}\right) \times \vec{\omega}\right]_x \\ &= \left(u_y - v_y\right)\omega_z , \end{aligned}$$

with the resulting terms being negative since the difference in fluid and bubble velocity is positive, and the vorticity in the z-direction is negative.

In comparing the turbulent and laminar boundary layer simulations, we find large differences in the overall behavior of the bubbles. The mean trajectory of the laminar boundary layer has bubbles traveling towards the wall, while the turbulent boundary layer shows the bubbles dispersing away from the wall as they travel downstream. The influence of the injection velocity is weak in both simulations, as the drag force quickly damps out the initial injection velocity. At this Reynolds number, the injection velocity of the bubbles can be ruled out as a mechanism for bubble dispersion away from the wall. The dispersion of bubbles away from the wall is dependent on the turbulence, with the fluid material derivative and drag forces on the bubble being strongly influential.

CONCLUSION

Experiments by Sanders *et al.* (2006) have shown that in high Reynolds number, spatially evolving turbulent boundary layers, microbubbles tend to migrate away from the wall as they travel downstream of injection and the skin-friction drag reduction approaches that of a single-phase turbulent boundary layer. We performed simulations of bubbles injected into a spatially evolving turbulent boundary layer using a one-way coupled Euler-Lagrangian approach. Though the Reynolds number of our simulation was lower than experiment, we observed bubbles moving away from the wall following injection due to each bubble's interaction with the surrounding turbulent flow. The forces on the bubbles were found to be intermittent, thus enhancing bubble dispersion. Bubbles injected into a laminar boundary layer traveled towards

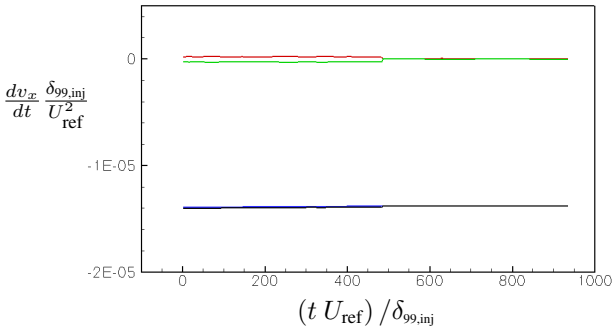

Figure 16: Bubble acceleration budget in the streamwise (x) direction for the laminar boundary layer simulation. —, Drag_x ; —, $3\frac{Du_x}{Dt}$; —, Lift_x; —, Total_x.

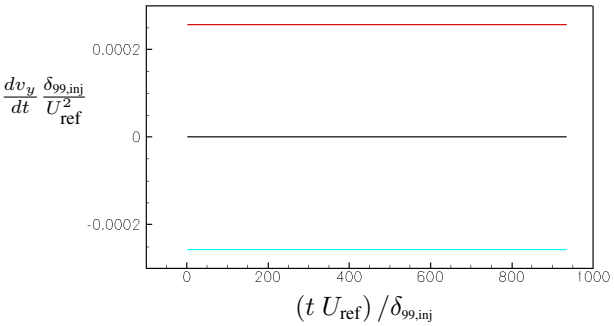

Figure 17: Bubble acceleration budget in the wall-normal (y) direction for the laminar boundary layer simulation. —, Drag_y; —, $-2g$; —, Total_y.

the wall, the opposite of what is found in our turbulent simulations and in the Sanders *et al.* (2006) experiment.

In our simulations we have assumed that the bubbles were small, solid, massless spheres with no modification of the turbulence by the bubbles and no interactions with other bubbles (the one-way coupled regime). Bubbles in a flow with a moderate cavitation number may change their radius in response to pressure fluctuations in the flow, though contaminates on the surface of microbubbles will restrict the radial mobility (Clift *et al.*, 1978). The bubble sizes in experiment are also not monodisperse but have a distribution of sizes. For simplicity, we have assumed a uniform bubble size equal to the mean, but accounting for non-uniform bubble size distribution may be important because the bubble drag and volumetric accelerations are functions of bubble size.

ACKNOWLEDGMENTS

This work is supported by the United States Office of Naval Research under ONR Grant N00014-07-1-0420 with Dr. Ki-Han Kim as technical monitor. Computing resources were provided by the Arctic Research Supercomputing Center, the Minnesota Supercomputing Institute, the San Diego Supercomputing Center and the Texas Advanced Computing Center.

NOMENCLATURE

ROMAN SYMBOLS

x, y, z	Coordinate axes, coordinates
Re	Reynolds number
Fr	Froude number
$\vec{g}$	Gravity vector
$\vec{x}$	Eulerian position vector
$R(t)$	Bubble radius
$d(t)$	Bubble diameter
$\vec{Y}(t)$	Bubble position vector
$\vec{u}(\vec{x},t)$	Fluid velocity vector
$\vec{v}(t)$	Bubble velocity vector
$p(\vec{x},t)$	Fluid pressure
m	Mass occupied by bubble
C_{D}	Drag coefficient
C_{L}	Drag coefficient
C_{M}	Added-mass coefficient
A_{b}	Bubble area (πR^2)
U	Reference velocity

GREEK SYMBOLS

ρ	Density
μ	Dynamic viscosity
ν	Kinematic viscosity
$\vec{\omega}(\vec{x},t)$	Vorticity vector
Δt	Timestep

SUBSCRIPTS

$(\ )_{\text{f}}$	of the carrier fluid, used as ρ_{f}
$(\ )_{\text{b}}$	of the bubble, used as m_{b}
$(\ )_{\text{e}}$	ensemble-averaged, used as $\langle\vec{u}\rangle_{\text{e}}$

ABBREVIATIONS

DNS	Direct Numerical Simulation
EL	Euler-Lagrangian
RP	Rayleigh-Plesset

References

[1] Auton, T.R., "The Lift Force on a Spherical Body in a Rotational Flow," J. Fluid Mech., Vol. 183, 1987, pp. 199-218.

[2] Auton, T.R., Hunt, J.C.R., and Prud'Homme, M., "The Force Exerted on a Body in Inviscid Unsteady Non-Uniform Rotational Flow," J. Fluid Mech., Vol. 197, 1988, pp. 241-257.

[3] Babu, P., "Simulation and Modeling of Three Turbulent Flow Problems," Ph.D. Thesis, 2007, Aerospace Engineering & Mechanics, University of Minnesota.

[4] Batchelor, G.K., An Introduction to Fluid Dynamics, Cambridge Univ. Press, Cambridge, UK, 1967, pp. 404-409.

[5] Clift, R., Grace, J.R., and Weber, M.E., Bubbles, Drops, and Particles, Academic, New York, 1978, pp. 171-202.

[6] Ferrante, A., and Elghobashi, S., "On the Physical Mechanisms of Drag Reduction in a Spatially Developing Turbulent Boundary Layer Laden with Microbubbles," J. Fluid Mech., Vol. 503, 2004, pp. 345-355.

[7] Ferrante, A., and Elghobashi, S., "Reynolds Number Effect on Drag Reduction in a Microbubble-Laden Spatially Developing Turbulent Boundary Layer," J. Fluid Mech., Vol. 543, 2005, pp. 93-106.

[8] Haberman, W.L. and Morton, R.K., "An Experimental Investigation of the Drag and Shape of Air Bubbles Rising in Various Liquids," DTMB Report 802, Sept. 1953.

[9] Johnson, V.E. Jr., and Hsieh, T., "The Influence of the Trajectories of Gas Nuclei on Cavitation Inception," 6th Naval Hydrodynamics Symp., 1966, pp. 163-179.

[10] Lhuillier, D., "Forces D'inertie Sur une Bulle en Expansion se Déplaçant Dans un Fluide," C. R. Acad. Sci. Paris Série II, Vol. 295, 1982, pp. 95-98.

[11] Lu, J., Fernández, A., and Tryggvason, G., "The effect of bubbles on the wall drag in a turbulent channel flow," Phys. of Fluids, Vol. 17, 095102, 2005.

[12] Lund, T.S., "Generation of Turbulent Inflow Data for Spatially-Developing Boundary Layer Simulations," J. Comp. Phys., Vol. 140, 1998, pp. 233-258.

[13] Mahesh, K., Constantinescu, G., and Moin, P., "A Numerical Method for Large-eddy Simulation in Complex Geometries," J. Comp. Phys., Vol. 197, 2004, pp. 215-240.

[14] Maxey, M.R., Chang, E.J., and Wang, L-P., "Interactions of Particles and Microbubbles with Turbulence," Exp. Thermal and Fluid Sci., Vol. 12, 1996, pp. 417-425.

[15] McCormick, M.E., and Bhattacharyya, R., "Drag Reduction of a Submersible Hull by Electrolysis," Naval Engrs. J., Vol. 85, No. 2, 1973, pp. 11-16.

[16] Sanders, W.C., "Bubble Drag Reduction in a Flat Plate Boundary Layer at High Reynolds Numbers and Large Scales," Ph.D. Thesis, 2004, Mechanical Engineering, University of Michigan.

[17] Sanders, W.C., Winkel, E.S., Dowling, D.R., Perlin, M., and Ceccio, S.L., "Bubble Friction Drag Reduction in a High-Reynolds-Number Flat-Plate Turbulent Boundary Layer," J. Fluid Mech., Vol. 552, 2006, pp. 353-380.

[18] Schlichting, H.T., Boundary Layer Theory., McGraw Hill, 1968, pp. 135-144.

[19] Simens, M.P., Jiménez, J., Hoyas, S., and Mizuno, Y., "A High-Resolution Code for Turbulent Boundary Layers," J. Comp. Phys., Vol. 228, 2009, pp. 4218-4231.

[20] Thomas, N.H., Auton, T.R., Sene, K., and Hunt, J.C.R., "Entrapment and Transport of Bubbles by Plunging Water," In Gas Transfer at Water Surfaces, ed. W. Brutsaert and G. H. Jirka, D. Reidel, 1984, pp. 255-268.

[21] Xu, J., Maxey, M.R., and Karniadakis, G., "Numerical Simulation of Turbulent Drag Reduction Using Micro-Bubbles," J. Fluid Mech., Vol. 468, 2002, pp. 271-281.